

MAGAZ3NE: Dust Deficiency in Ultramassive Quiescent Galaxies at $3 < z < 4$ with ALMA Observations

WENJUN CHANG ,¹ GILLIAN WILSON ,^{2,1} BEN FORREST ,³ IAN MCCONACHIE ,⁴ ALLISON NOBLE ,⁵ ADAM MUZZIN ,⁶ DANILO MARCHEZINI ,⁷ M. C. COOPER ,⁸ TRACY WEBB,⁹ GABRIELA CANALIZO ,¹ PERCY GOMEZ,¹⁰ YONGDA ZHU ,¹¹ ADIT HARIN EDWARD,⁶ HAN LEI ,⁹ AURELIEN HENRY ,² STEPHANIE M. URBANO STAWINSKI ,¹² AND M.E. WISZ 

¹Department of Physics and Astronomy, University of California, Riverside, 900 University Avenue, Riverside, CA 92521, USA

²Department of Physics, University of California, Merced, 5200 Lake Road, Merced, CA 95343, USA

³Department of Physics and Astronomy, University of California, Davis, One Shields Avenue, Davis, CA 95616, USA

⁴Department of Astronomy, University of Wisconsin-Madison, 475 N. Charter St., Madison, WI 53706 USA

⁵School of Earth and Space Exploration, Arizona State University, Tempe, AZ 85287, USA

⁶Department of Physics and Astronomy, York University, 4700, Keele Street, Toronto, ON M3J 1P3, Canada

⁷Department of Physics & Astronomy, Tufts University, MA 02155, USA

⁸Department of Physics and Astronomy, University of California, Irvine, 4129 Frederick Reines Hall, Irvine, CA 92697, USA

⁹Department of Physics, McGill Space Institute, McGill University, 3600 rue University, Montréal, Québec H3A 2T8, Canada

¹⁰W.M. Keck Observatory, 65-1120 Mamalahoa Hwy., Kamuela, HI 96743, USA

¹¹Steward Observatory, University of Arizona, 933 North Cherry Avenue, Tucson, AZ 85721, USA

¹²Department of Physics, University of California, Santa Barbara, Santa Barbara, CA 93106, USA

ABSTRACT

A major challenge in identifying massive quiescent galaxies at $z > 3$ is distinguishing truly passive systems from dust-obscured star-forming galaxies, as both populations exhibit similar red ultraviolet (UV)-to-near-infrared (NIR) colors. In this work, we present ALMA Band 7 dust-continuum observations of five ultramassive galaxies (UMGs; $\log(M_*/M_\odot) > 11$) spectroscopically confirmed at $z_{\text{spec}} > 3$ from the MAGAZ3NE survey. Our results reveal that only one galaxy shows a faint $870 \mu\text{m}$ dust continuum detection, while the remaining four UMGs are undetected down to the 3σ depth. By incorporating ALMA constraints into the spectral energy distribution analysis, we confirm that these UV-NIR-selected systems are truly quiescent UMGs, lying more than one dex below the star-forming main sequence with $\log(\text{sSFR/Gyr}^{-1}) < -1$, thereby ruling out the possibility of obscured star formation. We then estimate dust masses using both spectral energy distribution modeling and modified blackbody fitting, with consistent results between the two methods. We find that three UMGs have evolved into extremely dust-poor quiescent galaxies, with $M_{\text{dust}}/M_* \lesssim 10^{-4}$, while the ALMA-detected galaxy has a comparatively higher dust reservoir with $M_{\text{dust}}/M_* \sim 10^{-3}$. Our results present the most massive and extremely dust-poor spectroscopically confirmed quiescent galaxies known at $3 < z < 4$, providing valuable observational constraints on rapid dust removal and quenching processes in the early universe. Future molecular line observations will be essential to directly measure the gas content and verify the efficiency of the depletion process.

Keywords: Dust continuum emission (412) — Far infrared astronomy (529) — Galaxy evolution (594) — High-redshift galaxies (734) — Star formation (1569) — Galaxy quenching (2040)

1. INTRODUCTION

Over the last decade, deep optical and near-infrared surveys have revealed a growing population of massive galaxy candidates with quiescent spectral and photo-

metric properties at $z \gtrsim 1$ (e.g., R. Bezanson et al. 2019; L. Bugiani et al. 2025), and even up to $z > 3$ (e.g., S. Belli et al. 2014; K. Glazebrook et al. 2017; C. Schreiber et al. 2018a; B. Forrest et al. 2020a,b). With the advent of JWST, similar quiescent candidates have been reported at even higher redshifts (e.g., A. C. Carnall et al. 2023; S. M. Urbano Stawinski et al. 2024; S. Jin

et al. 2024; T. Nanayakkara et al. 2025; A. de Graaff et al. 2025; L. Bugiani et al. 2025). If these systems are genuinely quiescent at $z > 3$, their existence would imply that rapid mass assembly and efficient quenching occurred within the first 1-2 billion years of cosmic time, posing a significant challenge to current models of massive galaxy formation.

Most high-redshift candidates for massive quiescent galaxies (MQGs) have been identified primarily through near-infrared (NIR) spectroscopy and/or ultraviolet (UV)-NIR photometric surveys (e.g., C. Schreiber et al. 2018b; Z. C. Marsan et al. 2022; A. C. Carnall et al. 2023; B. Forrest et al. 2020b, 2024). This selection method has difficulty distinguishing truly quiescent systems from red, dust-obscured star-forming galaxies (SFGs), particularly at high redshift, especially for $z \gtrsim 3$, where rest-frame optical features shift into the NIR (A. Muzzin et al. 2013; Y.-H. Hwang et al. 2021). At these epochs, even Spitzer/MIPS 24 μm and JWST/MIRI probe rest-frame wavelengths that are too blue to trace thermal dust emission, leaving the possibility of contamination from dusty galaxies uncertain. Far-infrared (FIR) dust emission, such as that traced by ALMA, have revealed several such misclassifications, including the blended “Jekyll and Hyde” system at $z = 3.7$ (C. Schreiber et al. 2018a) and the dust-obscured case reported by W. Chang et al. (2025), illustrating that without high-resolution far-infrared data, the nature of many red galaxies at $z > 3$ remains ambiguous.

A multi-year Keck/MOSFIRE campaign, the “Massive Ancient Galaxies At $z > 3$ NEar-infrared” (MAGAZ3NE) survey (B. Forrest et al. 2020a, 2024), has been successful in spectroscopically confirming a sample of ultramassive galaxies (UMGs; $M_\star > 10^{11} \text{ M}_\odot$) with $3 \lesssim z_{\text{phot}} < 4$ (P. Saracco et al. 2020; B. Forrest et al. 2022, 2024; I. McConachie et al. 2022, 2025; W. Chang et al. 2025). Many MAGAZ3NE UMGs exhibit red spectral energy distributions (SEDs), and a subset show absorption features consistent with quiescence (B. Forrest et al. 2020a,b). The MAGAZ3NE spectroscopic sample has been characterized with multi-passband UV-to-NIR photometry and rest-frame optical spectroscopy. However, at such high redshifts, dust obscuration can suppress optical emission-line indicators of star formation, such as $[\text{OII}]\lambda\lambda 3726, 3729$, by reprocessing ionizing radiation from young stars into thermal emission in the rest-frame far-infrared (FIR). High-resolution ALMA observations are therefore crucial to definitively rule out the possibility of dust-obscured star formation in these sources and to mitigate potential photometric contamination from nearby sources (C. Schreiber et al. 2018a).

Recent ALMA studies have revealed a large diversity in the dust content of MQGs at $1 < z < 4$. Several galaxies exhibit substantial dust reservoirs relative to their stellar mass despite very low specific star-formation rates, implying that quenching can proceed inefficiently, with extended dust depletion timescales (R. Gobat et al. 2018; T. L. Suzuki et al. 2022; M. M. Lee et al. 2024). Conversely, other galaxies are undetected even in deep continuum observations, suggesting efficient removal or destruction of dust (K. E. Whitaker et al. 2021; R. Gobat et al. 2022; J. S. Spilker et al. 2025). The wide range of observed dust fractions may reflect a divergence in different quenching pathways or timescales, depending on whether the interstellar medium (ISM) is expelled by feedback or gradually consumed by residual star formation. In this work, we use ALMA Band 7 continuum imaging to study five spectroscopically confirmed UMGs from the MAGAZ3NE survey (B. Forrest et al. 2020b) that exhibit red UV-to-NIR SEDs and weak spectra features. The observations can provide direct measurements or upper limits on dust emission, breaking the degeneracy between truly quiescent and dust-obscured populations. It allows us to constrain the dust fraction and residual star formation, providing insight into the physical processes that drive massive galaxy quenching in the early Universe.

Our work is organized as follows. Section 2 summarizes the ALMA observations, data reduction, and the multi-wavelength photometric catalog. In Section 3, we describe the SED fitting procedures and the derivation of stellar properties. Section 4 examines whether the observed UMGs are truly quiescent. In Section 5, we discuss the inferred dust properties and their implications for quenching mechanisms. A summary of our conclusions is given in Section 6. Throughout this work, we assume a G. Chabrier (2003) initial mass function (IMF) and a Λ CDM cosmology with $H_0 = 70 \text{ km s}^{-1} \text{ Mpc}^{-1}$, $\Omega_M = 0.3$, and $\Omega_\Lambda = 0.7$. Finally, we utilize the AB magnitude system (J. B. Oke & J. E. Gunn 1983).

2. DATA

2.1. Target Selection

We selected ALMA targets from the MAGAZ3NE survey (B. Forrest et al. 2020b, 2024), which provided the spectroscopic follow-up sample of candidate high-redshift ultramassive galaxies at $z_{\text{phot}} \geq 3$ with a stellar mass of $\log(M_\star/M_\odot) > 11.0$. B. Forrest et al. (2020b) presented spectroscopically confirmed absorption-line UMGs at $z_{\text{spec}} > 3$ with UV-to-NIR SED-inferred star formation rates of at most a few $M_\odot \text{ yr}^{-1}$ (see details in Section 4 of B. Forrest et al. 2020b). The ALMA observations presented here target the four most quiescent

systems from this population, selected for their particularly low inferred star formation activity. These galaxies potentially experienced intense star formation episodes and rapid quenching. Four galaxies were observed with Keck/MOSFIRE in the H -band and K -band, with the exception of XMM-VID1-2075, which has only K -band coverage, targeting the expected positions of the $H\beta$ and $[\text{OII}]$ emission lines.

2.2. ALMA Observation and Reduction

Band 7 (872 μm) continuum observations of four targeted sources were carried out in the Cycle 8 program (Project ID: 2021.1.00501.S, PI: B. Forrest). We obtained the calibrated measurement sets (MSs) from the National Radio Astronomy Observatory (NRAO), which were calibrated using Pipeline version 2021.2.0.128.¹³ Three XMM-VIDEO targets were observed using the ALMA 12-meter array, which has 61 antennas and successfully passed the QA2 quality level. The scheduling block for target COS-DR3-201999 timed out due to the end of the observation cycle. This target was observed using the 12-meter array with 42 antennas. In addition to the four UMGs selected for ALMA observations, the ALMA field of view (FoV) includes an additional MAGAZ3NE UMG in the COSMOS field, COS-DR3-202019 ($z_{\text{spec}} = 3.133$), located 7.4'' from COS-DR3-201999 ($z_{\text{spec}} = 3.131$). This source was previously identified in B. Forrest et al. (2020b) as an $[\text{OII}]$ emitting, star-forming galaxy based on its rest-frame optical spectra and UV-NIR photometry. Given its inclusion in the FoV, we incorporate it into our analysis to investigate its dust properties. In total, this work analyzes five UMGs, including the four originally selected ALMA targets and COS-DR3-202019.

We further processed and reduced the data for all sources with the version 6.6.3.22 package of Common Astronomy Software Application (**CASA**). The calibrated visibilities were imaged using the **TCLEAN** algorithm in **CASA**, with natural weighting (**ROBUST** = 2) and pixel scales of 0.05'' for XMM targets and 0.08'' for COSMOS targets. The images were cleaned to the Root Mean Square (RMS) noise of 11.7–18.6 $\mu\text{Jy beam}^{-1}$. Three XMM targets achieve an RMS noise level consistent with the expected 14 $\mu\text{Jy beam}^{-1}$, while the COSMOS observations are slightly less sensitive due to the reduced exposure time. We then applied task **imfit** in **CASA** to measure the integrated fluxes for all UMGs and deconvolved beam sizes (FWHM) through a two-dimensional (2D) Gaussian fitting procedure. Only UMG XMM-VID3-2457 is detected in Band 7 continuum with a flux

of $294 \pm 33 \mu\text{Jy}$, while the remaining four targets are undetected down to the RMS sensitivity.

Figure 1 shows the 872 μm continuum emission for the only detected source, XMM-VID3-2457, together with the best-fit 2D Gaussian model and the corresponding residual map. No region exhibits a significant excess beyond 3σ . The remaining four UMGs are individually undetected at the 3σ level in the ALMA continuum maps. In order to verify the absence of significant emission, we construct a stacked continuum image after convolving all maps to the lowest angular resolution in the sample, that of COS-DR3-201999. The stacking is performed using inverse-variance weighting based on the local RMS noise measured in the primary-beam-uncorrected images. The resulting stacked image is shown in the right panel of Figure 1, reaches an rms sensitivity of $\sigma_{\text{stack,RMS}} = 8.0 \mu\text{Jy beam}^{-1}$, and does not reveal any significant continuum emission. Table 1 provides the observational parameters and the processed data for five UMGs. During the SED fitting in Section 3, we adopt 3σ upper limits on the ALMA band 7 photometry for the UMGs without detections.

2.3. UV-to-NIR Photometry

Three ultramassive galaxies were selected in the XMM-Newton Large Scale Structure field from the VISTA Deep Extragalactic Observations survey (VIDEO; M. J. Jarvis et al. 2013). This field was divided into three VIDEO survey tiles (XMM-VID1, VID2, and VID3), distinguishing sources by their location within the survey. The photometric catalog was constructed using VIDEO DR4 data over 4.65 deg^2 with a 5σ depth of $K_s = 23.8 \text{ mag}$ (B. Forrest et al. 2020b; Annunziatella et al. 2026, in prep.). These contain 22 photometric passbands ranging from u band to IRAC 8.0 μm , including deep near-IR observations at Z -, Y -, H -, and K_s -band from the VIDEO survey (M. J. Jarvis et al. 2013), deep IRAC data from SERVS (J. C. Mauduit et al. 2012) and the Deep Drill survey (M. Lacy et al. 2021).

Two additional UMGs were selected from the Ultra-VISTA near-infrared imaging survey (H. J. McCracken et al. 2012), which covers the COSMOS field (N. Scoville et al. 2007). The K_s -selected photometric catalog (Z. C. Marsan et al. 2022) was constructed with *ultra-deep* UltraVISTA imaging Data Release 3 (hereafter DR3) covering 0.84 deg^2 and reaching a depth of 5σ of $K_s = 25.2 \text{ mag}$ within a 2''.1 diameter aperture, following the same methodology as described in A. Muzzin et al. (2013). The DR3 catalog provides ancillary photometry spanning 0.15–24 μm across 49 bands, with “COS-DR3” denoting sources from the UltraVISTA DR3 catalog.

¹³ Download MS from NRAO: <https://data.nrao.edu/portal/>

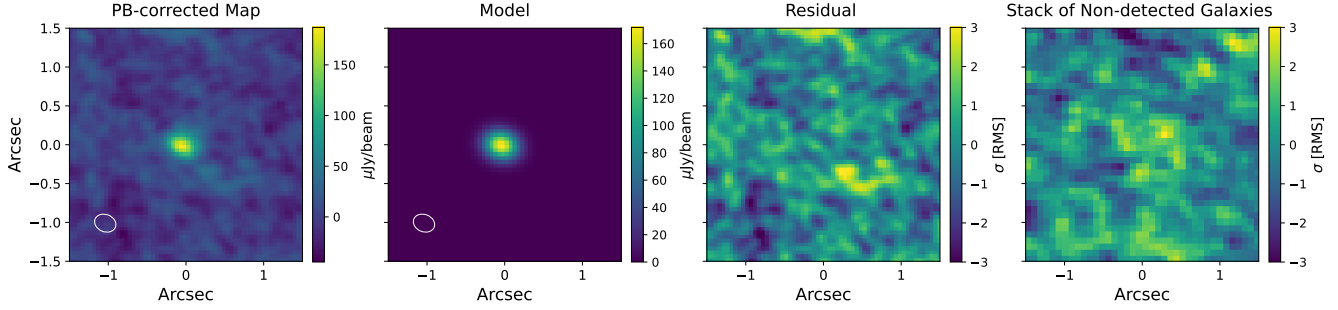


Figure 1. From left to right: ALMA Band 7 (870 μm) primary-beam-corrected continuum image of XMM-VID3-2457; the two-dimensional Gaussian model; the residual map after subtraction of the model, shown in units of the RMS; and the stacked continuum image of four non-detected galaxies. The $0.28'' \times 0.22''$ synthesized beam of XMM-VID3-2457 is represented by the white ellipse at the bottom left corners.

Table 1. ALMA band 7 (872 μm) observation parameters. Flux density is estimated from pb-corrected images using `imfit` task.

Object	z_{spec}	Int. Time (s)	Flux (μJy)	RMS ($\mu\text{Jy beam}^{-1}$)	Beam Size	QA2 status
XMM-VID3-2457	$3.498_{-0.002}^{+0.003}$	8437	294 ± 33	12.6	$0.28'' \times 0.22''$, PA = 68°	PASS
XMM-VID3-1120	$3.492_{-0.003}^{+0.002}$	8437	< 35.1 (3σ)	11.7	$0.28'' \times 0.22''$, PA = 68°	PASS
XMM-VID1-2075	$3.495_{-0.002}^{+0.001}$	8437	< 35.4 (3σ)	11.8	$0.28'' \times 0.22''$, PA = 68°	PASS
COS-DR3-201999	$3.131_{-0.001}^{+0.001}$	2873	< 55.8 (3σ)	18.6	$0.42'' \times 0.29''$, PA = 70°	SEMPASS
COS-DR3-202019 ^a	$3.133_{-0.001}^{+0.002}$	2873	< 55.8 (3σ)	18.6	$0.42'' \times 0.29''$, PA = 70°	SEMPASS

^aCOS-DR3-202019 lies within the primary beam of the COS-DR3-201999 pointing.

Figure 2 shows the rest-frame U - V and V - J (RF UVJ ; hereafter) colors of the five UMGs, together with other spectroscopically-confirmed MAGAZ3NE UMGs (B. Forrest et al. 2020b) and Super-UMG candidates ($M_{\text{phot}} > 10^{11.7} M_\odot$; B. Forrest et al. 2024). The RF colors were derived from UV-to-8 μm photometry fit with FAST++ at the spectroscopic redshift of each galaxy, where the K -band flux was corrected for emission line fluxes (for full details, see B. Forrest et al. 2020b). As shown in the figure, all five UMGs lie securely within the quiescent wedge of the UVJ diagram (K. E. Whitaker et al. 2011). This placement suggests that they are consistent with quiescent population, rather than dusty star-forming galaxies. Our comparison with massive galaxies with $\log(M_\star/M_\odot) > 10.5$ at $3 < z_{\text{phot}} < 4$ from the COSMOS2020 catalog (J. R. Weaver et al. 2022) shows no clear bimodality in Figure 2.

2.4. Ancillary Photometry in the COSMOS Field

For the two UMGs in this work that lie in the COSMOS field, which benefit from extensive multi-wavelength coverage, we complement the UltraVISTA DR3 photometric catalog with an IR-to-radio deblended

photometric catalog (S. Jin et al. 2018, hereafter as Jin18). Detailed cross-matching between these catalogs is described in W. Chang et al. (2025). The Jin18 catalog employs prior-based deblending techniques to mitigate the effects of source confusion and blending caused by the large beam sizes of FIR observations. The two COSMOS UMGs in this work are matched to sources in the Jin18 catalog using their DR3 coordinates, with a positional offset $\leq 0.2''$. We adopt the *Spitzer*/MIPS 24 μm (PI: D. Danders; E. Le Floc'h et al. 2009) and VLA 3 GHz and 1.4 GHz (V. Smolčić et al. 2017; E. Schinnerer et al. 2010) photometry from Jin18. *Herschel* and SCUBA2 data are excluded because the environments of COS-DR3-202019 and COS-DR3-20199 are highly crowded, with over ten bright K_s -band sources within $10''$, well below the *Herschel* (FWHM $\sim 7''$ - $36''$) and SCUBA2 850 μm (FWHM $\sim 11''$) beam sizes. For COS-DR3-201999, no radio counterpart is reported in the VLA catalog of V. Smolčić et al. (2017). To avoid adopting a potentially uncertain deblended flux, we instead derive a radio upper limit directly from the VLA 3 GHz and 1.4GHz images. The RMS noises are measured

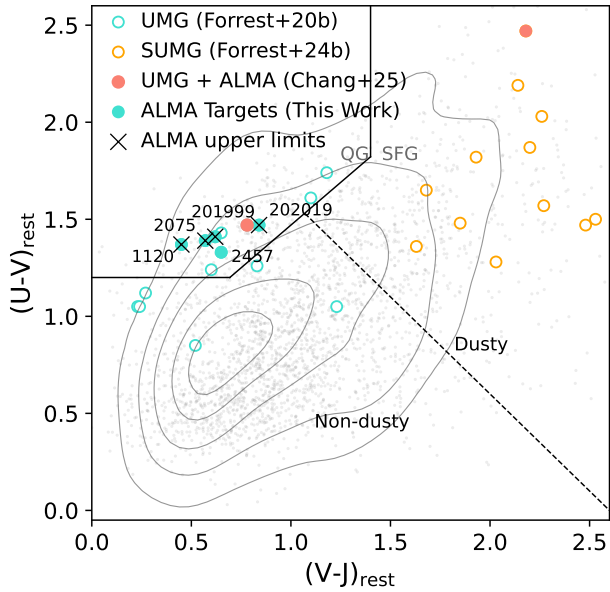


Figure 2. Rest-frame (RF) UVJ color-color diagram for 16 spectroscopically-confirmed UMG candidates (open cyan circles) presented in B. Forrest et al. (2020b) and 12 spectroscopically-confirmed S-UMGs candidates (open orange circles) presented in B. Forrest et al. (2024). The five UMGs from B. Forrest et al. (2020b) observed with ALMA in this work are shown by filled cyan circles (Galaxy 1: XM-M-VID3-2457; 2: XM-M-VID3-1120; 3: XM-M-VID1-2075; 4: COS-DR3-201999; 5: COS-DR3-202019), where cross symbols indicate non-detections in ALMA dust continuum with upper limits only. Two additional ALMA-detected UMGs analyzed previously in W. Chang et al. (2025) are shown as filled salmon circles. The RF colors were estimated at the spectroscopic redshift using FAST++ and UV-to- $8\mu\text{m}$ photometry only. The dashed line denotes the division between “dusty” and “non-dusty” star-forming regions (C. Schreiber et al. 2018b). The gray data points corresponds to massive galaxies with $\log(M_*/M_\odot) > 10.5$ at $3 < z_{\text{phot}} < 4$ in the COSMOS2020 catalog (J. R. Weaver et al. 2022), with their density distribution overplotted as gray contours.

in source-free regions near the target using Cube Analysis and Rendering Tool for Astronomy (CARTA), and the resulting value is used to define the corresponding (3σ) upper limit.

3. SED FITTING

To investigate the dust content and star formation activity of these high- z UMGs, we perform multi-wavelength SED fitting with CIGALE (Code Investigating GALaxy Emission)¹⁴, a flexible energy balance SED

modeling code that relies on Bayesian inference to estimate the physical properties of galaxies (M. Boquien et al. 2019; G. Yang et al. 2020, 2022). In this framework, the stellar light absorbed by dust at UV-NIR wavelengths are redistributed and emitted consistently in the MIR and FIR. Here, we briefly describe the modules used to fit the SEDs for our sample. Full details of input parameters may be found in Table A.1. We adopt a delayed exponentially declining star formation history (SFH) and simple stellar populations (SSPs) from G. Bruzual & S. Charlot (2003), assuming a G. Chabrier (2003) IMF. Nebular emission is included, parameterized by the ionization parameter and gas-phase metallicity. We employ the dust modified attenuation law of D. Calzetti et al. (2000) and the dust emission templates of B. T. Draine et al. (2014). AGN emission is modeled using the clumpy SKIRTOR framework (M. Stalevski et al. 2012, 2016), including viewing representing face-on (type 1) and edge-on (type 2) AGN. As noted in Section 2.4, COS-DR3-201999 and COS-DR3-202019 are detected at VLA 3 GHz and 1.4 GHz. For these two UMGs across UV-to-radio range, we additionally include the radio module to account for a power-law synchrotron spectrum and AGN radio emission.

The best-fit SEDs and imaging of K_s band and ALMA band 7 for five UMGs are presented in Figure 3, alongside a comparison with the H - and/or K -band spectra observed by Keck/MOSFIRE, which demonstrate a high level of consistency between the best-fit model and the spectroscopic data. The Bayesian-derived properties of the five UMGs from the CIGALE SED fitting are summarized in Table 2, together with the stellar properties obtained using FAST++ (C. Schreiber & H. Dickinson 2023) as reported in B. Forrest et al. (2020b), and SFRs derived from multiple tracers. B. Forrest et al. (2020b) reported stellar masses and SFRs for MAGAZ3NE UMGs using FAST++ fits to the UV-NIR photometry and spectroscopy, performed without AGN templates. The stellar masses obtained from FAST++ and CIGALE are consistent within 0.1 dex for four of the ALMA-targeted UMGs. The only exception is COS-DR3-202019, a close companion of COS-DR3-201999, for which CIGALE derives a stellar mass lower by ~ 0.25 dex. This offset potentially reflects the inclusion of AGN and radio components in the CIGALE modeling, which are not accounted for in the FAST++ fits, which we discuss in Section 4.3. In the following sections, we adopt the CIGALE-derived results to discuss the star-formation activity and dust emission properties of these five UMGs (Sections 4 and 5).

¹⁴ CIGALE v2022.1: <https://cigale.lam.fr/>

Table 2. Physical properties for five UMGs.

ObjID	Method	XMM-VID3-2457	XMM-VID3-1120	XMM-VID1-2075	COS-DR3-201999	COS-DR3-202019
redshift	EAZY	$3.51^{+0.07}_{-0.07}$	$3.40^{+0.12}_{-0.10}$	$3.48^{+0.08}_{-0.07}$	$3.14^{+0.09}_{-0.09}$	$3.10^{+0.06}_{-0.04}$
	slinefit	$3.498^{+0.003}_{-0.002}$	$3.492^{+0.002}_{-0.003}$	$3.452^{+0.001}_{-0.002}$	$3.131^{+0.001}_{-0.001}$	$3.133^{+0.002}_{-0.001}$
Stellar Properties						
log M_{\star} [M_{\odot}]	F20b	$11.26^{+0.02}_{-0.03}$	$11.47^{+0.02}_{-0.03}$	$11.52^{+0.00}_{-0.05}$	$11.40^{+0.03}_{-0.01}$	$11.67^{+0.04}_{-0.05}$
	CIGALE	$11.25^{+0.06}_{-0.07}$	$11.51^{+0.02}_{-0.02}$	$11.50^{+0.03}_{-0.03}$	$11.33^{+0.02}_{-0.03}$	$11.49^{+0.05}_{-0.05}$
SFR [M_{\odot} yr $^{-1}$]	F20b	< 0.4	< 0.1	< 1.0	$1.3^{+0.3}_{-1.2}$	$82.4^{+10.4}_{-58.2}$
	CIGALE	8.7 ± 4.1	4.1 ± 2.2	4.9 ± 2.8	1.1 ± 0.7	18.1 ± 2.1
	L_{IR}	12.6 ± 4.1	8.4 ± 3.0	9.7 ± 4.3	3.8 ± 0.6	7.4 ± 1.1
	$H\beta$	2.2 ± 3.8	4.2 ± 4.9	9.1 ± 2.2	1.5 ± 2.5	36.5 ± 13.3
	[O II]	2.5 ± 1.9	2.8 ± 2.3	—	6.3 ± 1.2	57.6 ± 2.6
log sSFR [yr $^{-1}$]	F20b	< -11.63	< -12.44	< -11.47	$-11.29^{+0.09}_{-1.11}$	$-9.75^{+0.07}_{-0.53}$
	CIGALE	$-10.31^{+0.23}_{-0.33}$	$-10.90^{+0.21}_{-0.35}$	$-10.81^{+0.23}_{-0.39}$	$-11.27^{+0.23}_{-0.42}$	$-10.24^{+0.10}_{-0.10}$
A_V	F20b	0.5 ± 0.02	0.0 ± 0.0	0.4 ± 0.2	0.4 ± 0.1	0.6 ± 0.3
	CIGALE	0.10 ± 0.05	0.05 ± 0.02	0.04 ± 0.02	0.03 ± 0.01	0.03 ± 0.01
fracAGN	CIGALE	0.16 ± 0.11	0.14 ± 0.09	0.11 ± 0.05	0.50 ± 0.10	0.47 ± 0.10
Dust Properties						
log L_{dust} [L_{\odot}]	CIGALE	$11.10^{+0.17}_{-0.12}$	$10.93^{+0.13}_{-0.19}$	$10.98^{+0.16}_{-0.25}$	$10.58^{+0.07}_{-0.08}$	$10.87^{+0.06}_{-0.07}$
log M_{dust} [M_{\odot}]	CIGALE	$8.43^{+0.15}_{-0.22}$	$7.14^{+0.15}_{-0.23}$	$7.23^{+0.13}_{-0.28}$	$7.40^{+0.22}_{-0.48}$	$7.42^{+0.15}_{-0.23}$
	MBB	$8.22^{+0.05}_{-0.05}$	< 7.30	< 7.30	< 7.49	< 7.49

4. SUPPRESSED STAR FORMATION IN UMGs

4.1. Star-Forming Main Sequence

With the inclusion of ALMA data into the UV-to-FIR SED fitting, we present the CIGALE-derived stellar mass and $\text{SFR}_{10\text{Myrs}}$ of five UMGs with the star-forming main sequence (SFMS) at $z = 3.5$ in Figure 4. Filled circles represent UV-to-FIR SED fits from this work, while orange filled circles indicate the two MAGAZ3NE UMGs (COS-DR3-195616 and COS-DR1-209435) previously analyzed with UV-to-FIR SED fitting by [W. Chang et al. \(2025\)](#) including ALMA observations. All five UMGs lie significantly (> 1 dex) below the SFMS ($\Delta \log \text{SFR} < -1$) from [A. R. Tomczak et al. \(2016\)](#), classifying them as quiescent systems at $z > 3$. Figure 4 compares the SED-derived quantities of other spectroscopically confirmed quiescent galaxies at $3 < z < 4$ observed with ALMA presented by [M. Kubo et al. \(2022\)](#) fitted with CIGALE. The five MAGAZ3NE UMGs occupy the ultramassive regime ($\log(M_{\star}/M_{\odot}) > 11.2$), where spectroscopically confirmed systems remain rare.

4.2. Specific Star Formation Rate

The CIGALE-derived specific star formation rates (sSFRs) of our sample are all below $\log(\text{sSFR}_{\text{MS}}/\text{Gyr}^{-1}) < -1$ (Table 2), placing them well

below the star-forming main sequence and confirming their quiescence. In Figure 5, we compare sSFRs of our UMGs with several important tracers. We derive SFRs from the total dust luminosity (L_{dust}) obtained from SED modeling, which quantifies the energy re-emitted by interstellar dust grains after disentangling and removing the contribution from AGN heating. L_{dust} is then converted to SFR using the [R. C. Kennicutt \(1998\)](#) calibration adjusted for a [G. Chabrier \(2003\)](#) IMF. We note that L_{dust} may include a contribution from dust heated by evolved stellar populations, especially in quiescent or post-starburst systems. The line-based SFRs are adopted from [B. Forrest et al. \(2020b\)](#) and are estimated from the $H\beta$ and [O II] luminosities using line fluxes measured with [slinefit](#) ([C. Schreiber 2023](#)). XMM-VID3-2457, the only source with an ALMA detection, shows slightly elevated sSFRs from the SED fitting and L_{IR} relative to those inferred from the nebular emission lines, likely indicating a modest amount of dust-obscured star formation consistent with the detected thermal dust emission detected by ALMA. Nevertheless, the sSFR estimates remain consistent within 1σ under the threshold of $\log(\text{sSFR}/\text{Gyr}^{-1}) < -1$, and therefore still satisfies our quiescent selection criteria. The ALMA detection thus does not preclude its classi-

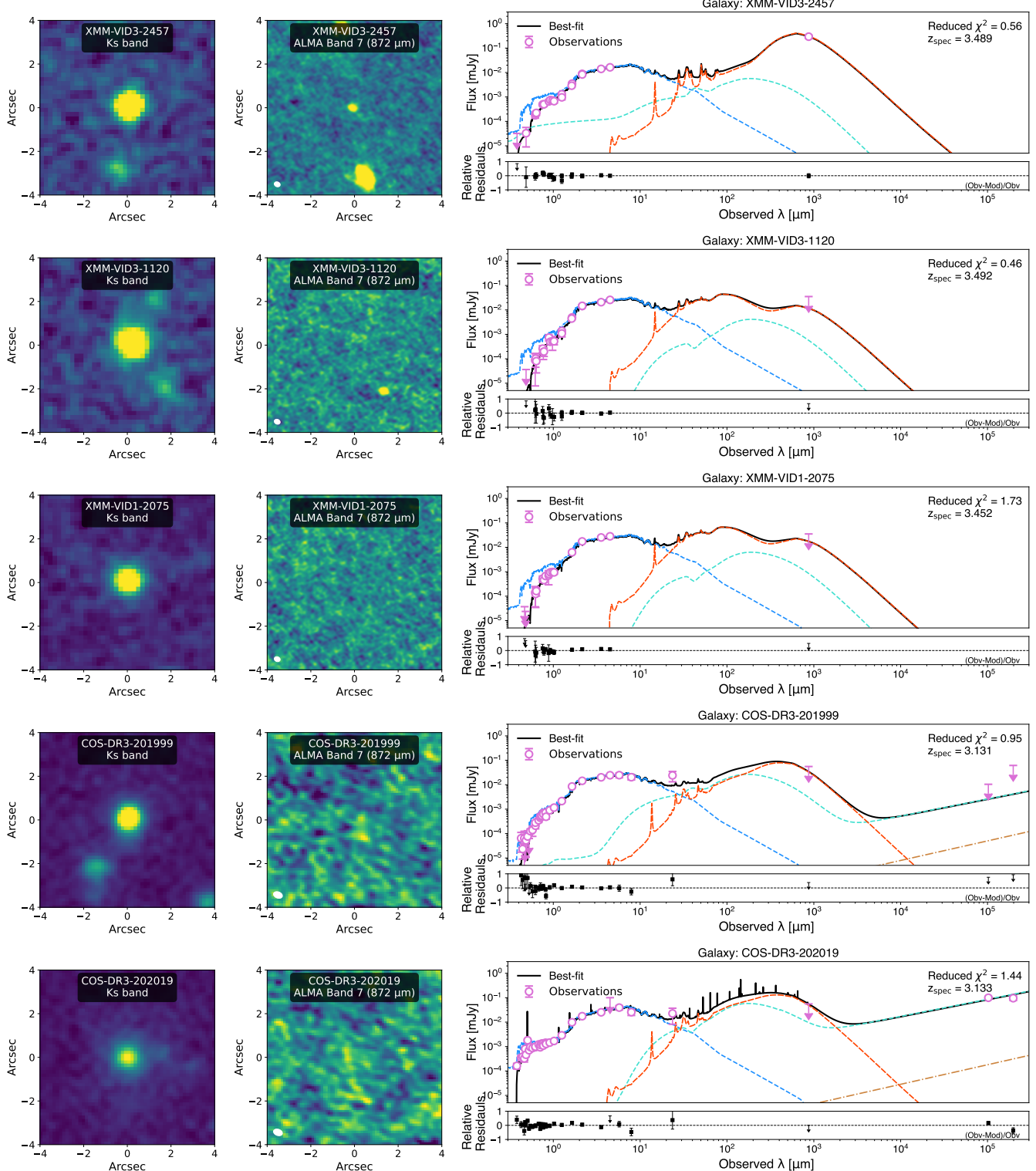


Figure 3. K_s -band images, ALMA band 7 ($872\mu\text{m}$) primary-beam-corrected continuum maps, and UV-to-millimeter/radio SED modeling of the five UMGs. Imaging cutouts are centered on the spectroscopic positions of the galaxies. White ellipses in the lower-left corners of the ALMA maps show the synthesized beam. The SED panels on the right show the best-fit model (top) and relative residuals (bottom). Dashed lines indicate the individual CIGALE SED components: unattenuated stellar emission (blue), dust emission (red), and AGN emission (cyan). For UMGs COS-DR3-201999 and COS-DR3-202019, an additional synchrotron radio emission component is included (brown). Observed photometry is shown as purple circles, with downward arrows indicating upper limits.

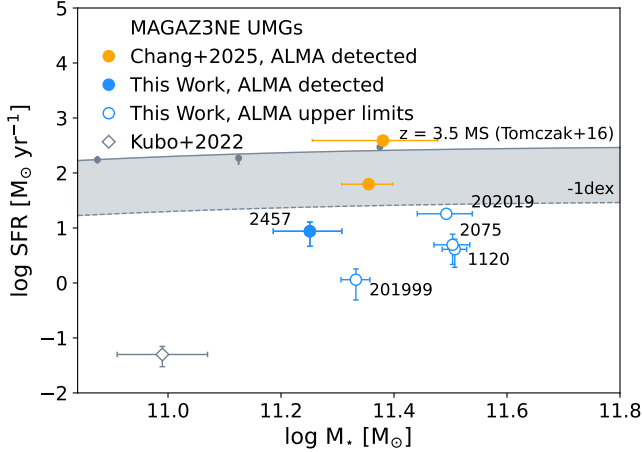


Figure 4. The SFR versus stellar mass. Blue filled circles show the CIGALE-derived measurements for the five UMGs in this work, while open circles mark UMGs with ALMA upper limits only. Gray symbol represents the spectroscopically confirmed quiescent galaxy at $3 < z < 4$ observed with ALMA and fitted with CIGALE in M. Kubo et al. (2022). The gray line shows the star-forming main sequence from A. R. Tomczak et al. (2016). Shaded regions denote 1 dex below the SFMS, corresponding to the threshold for classifying galaxies as quiescent comparing to the main sequence. Orange filled circles represent two MAGAZ3NE UMGs analyzed using UV-to-FIR CIGALE SED with ALMA observations in W. Chang et al. (2025).

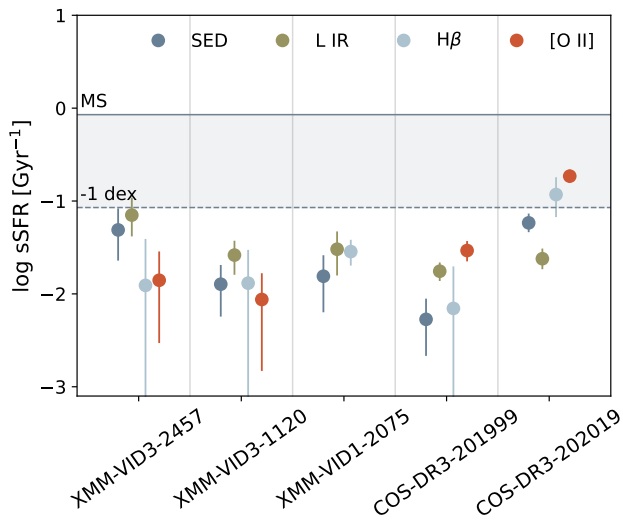


Figure 5. Comparison of sSFR estimates from different sources: CIGALE SED fitting (dark blue), L_{IR} (olive), $H\beta$ (light blue), $[\text{OII}]$ (red). We adopt the A. R. Tomczak et al. (2016) relation to calculate the expected sSFR for main-sequence UMGs ($\log(M_*/M_\odot) = 11.5$), $\log s\text{SFR}_{\text{MS}}/\text{Gyr}^{-1} = -0.07$. The region between the main sequence value and 1 dex below is highlighted in gray.

fication as quiescent, but rather indicates the presence of weak, dust-obscured star formation in an otherwise quiescent UMG.

The other two XMM-field UMGs, XMM-VID3-1120 and XMM-VID1-2075, show no ALMA detection. This lack of significant dust emission is consistent with their low sSFRs derived from other tracers, confirming that they are robustly quiescent systems with $\log(\text{sSFR}/\text{Gyr}^{-1}) < -1.5$ below the SFMS. Even though COS-DR3-201999 shows strong AGN signatures ($\text{frac}_{\text{AGN}} > 0.4$; see Table 2), its SFRs remain well below the star-forming main sequence, indicating that the galaxy is quenched and the AGN activity is dominated by radio emission (see Figure 3 and Section 4.3). In contrast, COS-DR3-202019 display moderately elevated sSFRs inferred from $H\beta$ and $[\text{OII}]$ relative to SED- or L_{IR} -based values, approaching the -1 dex threshold. As seen in the figure, the sSFR derived from $[\text{OII}]$ is higher by over 0.5 dex compared to the SED fit. COS-DR3-202019 was first reported in (B. Forrest et al. 2020b) with a large uncertainty on estimation of SFR with $82.4^{+10.4}_{-58.2} M_\odot/\text{yr}$. However, its ALMA non-detection rules out dusty obscured star formation, and its radio emission is likely associated with AGN activity (see Section 4.3). While the strong emission of $[\text{OII}]$ and $H\beta$ could be produced from unobscured star formation, it could also arise from the narrow-line region of an AGN. With the AGN contribution inferred from SED and the non-negligible radio AGN emission, we therefore caution that the SFRs from the line fluxes for COS-DR3-202019 could be significantly overestimated.

4.3. AGN Contribution

We utilize the SKIRTOR module in CIGALE to estimate the AGN fraction, frac_{AGN} , defined as $L_{\text{dust,AGN}}/(L_{\text{dust,AGN}} + L_{\text{dust,galaxy}})$. The two UMGs in the COSMOS field, COS-DR3-202019 and COS-DR3-201999, exhibit substantial AGN contribution (CIGALE-derived $\text{frac}_{\text{AGN}} > 0.45$), while the other three UMGs in the XMM-field show faint AGN contributions with $\text{frac}_{\text{AGN}} < 0.2$. COS-DR3-202019 shows strong detections at both 1.4 and 3 GHz ($\text{S/N} > 3$), while COS-DR3-201999 is constrained by radio upper limits. With a spectral index of $\alpha = -0.8$ (Z. C. Marsan et al. 2017), we derive $L_{1.4\text{GHz}} < 4.0 \times 10^{24} \text{ W Hz}^{-1}$ for COS-DR3-201999 and the luminosity of $L_{1.4\text{GHz}} = (6.2 \pm 1.2) \times 10^{24} \text{ W Hz}^{-1}$ for COS-DR3-202019 following the equation from A. Butler et al. (2018). In addition, the radio-loudness parameter from CIGALE radio module, defined as $R_{\text{AGN}} = L_{\nu, 5\text{GHz}}/L_{\nu, 2500\text{\AA}}$, is 19 ± 10 for COS-DR3-201999 and higher for COS-DR3-202019 (144 ± 45),

Table 3. AGN classification.

UMG	f_{AGN}	R_{AGN}	$L_{1.4\text{GHz}}$	Line Ratio
			$(10^{24} \text{ W Hz}^{-1})$	$f_{[\text{OIII}]\lambda 5007}/f_{H\beta}$ ^a
X-2457	0.16 ± 0.11	–	–	7.0 ± 12.3
X-1120	0.14 ± 0.09	–	–	-5.2 ± 6.3
X-2075	0.11 ± 0.05	–	–	0.6 ± 0.8
C-201999	0.50 ± 0.10	> 10	< 4	8.7 ± 14.9
C-202019	0.47 ± 0.10	> 100	6.2 ± 1.2	1.0 ± 0.4

^a $f_{[\text{OIII}]\lambda 5007}/f_{H\beta} > 6$, consistent with AGNs at these large stellar masses.

both exceeding the conventional threshold of $R_{\text{AGN}} > 10$ (G. Yang et al. 2022) and identifying them as radio-loud AGN, indicative of the powerful AGN jets.

To assess the role of AGN emission in the UV-to-radio SEDs for two COS-UMGs, we rerun the SED fitting excluding AGN module while while keeping all other model components and parameter ranges identical to those in Section 3. As shown in Figure A.1, the non-AGN models underpredict the observed radio flux, indicating a radio excess relative to stellar processes alone, whereas the inclusion of an AGN component reproduce fits more accurately. It confirms that the radio emission in two COS-UMGs, particularly COS-DR3-202019 with robust radio detections, is dominated by an AGN rather than residual star formation. In B. Forrest et al. (2020b), [OIII] and H β emission lines were tentatively detected in the MOSFIRE K -band spectrum of COS-DR3-201999, while the H β feature is highly uncertain due to the low signal-to-noise. The MOSFIRE spectra of the remaining XMM-field targets are dominated by stellar absorption features, with no robust detections of nebular emission lines. The corresponding line ratios are listed together with other AGN indicators in Table 3. The AGN identification for the two COSMOS UMGs is mainly driven by their radio and SED properties. Their weak spectral line constraints are consistent with a low-excitation, jet-dominated AGN mode, as observed in low-excitation radio galaxies (LERGS, A. Butler et al. 2018).

5. DUST PROPERTIES

5.1. SED-derived Dust Mass

We estimate dust masses using the B. T. Draine et al. (2014) dust emission models in CIGALE. This model accounts for both diffuse interstellar dust heated by the general stellar population and dust in star-forming regions exposed to a range of radiation fields ($U_{\text{min}}-U_{\text{max}}$). The parameters γ and q_{PAH} control the fraction of warm dust and small aromatic grains, allowing a consistent

derivation of total dust mass. We present dust mass ($M_{\text{dust,SED}}$) and dust luminosities (L_{dust}) for five UMGs in Table 2, where L_{dust} is adopted to estimate SFR_{IR} in Section 4.2). The ALMA-detected source shows the highest dust mass with $\log(M_{\text{dust}}/M_{\odot}) = 8.43^{+0.15}_{-0.22}$, whereas the remaining galaxies have significantly lower values with $\log(M_{\text{dust}}/M_{\odot}) < 8$, listed in Table 2.

5.2. Modified Blackbody Dust Mass

Another efficient method for estimating dust mass from the single-band FIR detection is to apply a modified blackbody (MBB) fit. We determine dust masses according to the following equation:

$$M_{\text{dust}} = \frac{D_L^2 S_{\nu_o}}{(1+z) \kappa_{\nu_r}} [B_{\nu_r}(T_d) - B_{\nu_r}(T_{\text{CMB}}(z))]^{-1},$$

where S_{ν_o} is the flux density at the ALMA observed frequency (345 GHz for band 7) with $\nu_o = \nu_r(1+z)^{-1}$. We adopt $\kappa_{\nu_r} = \kappa_0(\lambda_0/\lambda_{\text{rest}})^{\beta}$, assuming a dust mass opacity coefficient κ_0 of $0.0431 \text{ m}^2 \text{ kg}^{-1}$ at $\lambda_0 = 850\mu\text{m}$ (A. Li & B. T. Draine 2001), and a dust emissivity index β of 1.8 (N. Scoville et al. 2014). $T_{\text{CMB}}(z) = 2.725 \times (1+z)$ is the CMB temperature at redshift z , which affects the derived dust mass by $\sim 5\%$ (≈ 0.02 dex). The B. T. Draine et al. (2014) dust emission fits the effective dust temperature of $T_d \sim 22 - 33$ K for our UMGs. We adopt a representative value of $T_d = 25$ K for the following analysis, which is consistent with the assumptions used for the literature MQGs compared in Section 5.3. For the four UMGs without ALMA detections, the values of S_{ν_o} correspond to 3σ upper limits, and the derived M_{dust} is also considered as upper limits. The estimated dust masses are shown in Table 2.

We compare MBB- and SED-derived dust masses in Fig. 6, which are broadly consistent. The robust MBB detection (XMM-VID3-2457) lies essentially on the 1:1 relation within 0.3 dex, indicating no obvious systematic offset in the SED-based dust mass scale. For the remaining galaxies, the MBB constraints are upper limits derived from ALMA non-detections, and all fall at or slightly above the SED estimates. Overall, we find no significant discrepancy between the two methods, with differences within $\lesssim 0.3$ dex. The lower SED-derived dust masses for the two COSMOS targets, COS-DR3-201999 and COS-DR3-202019, are encompassed by the MBB-derived upper limits. In the following section, we utilize the MBB-derived dust masses and corresponding upper limits to discuss the dust content of our sample, including both detected and non-detected UMGs.

5.3. Extremely Dust-poor MQGs

In Figure 7 (left), we show the dust-to-stellar mass ratio ($M_{\text{dust}}/M_{\star}$) for five UMGs, derived from MBB

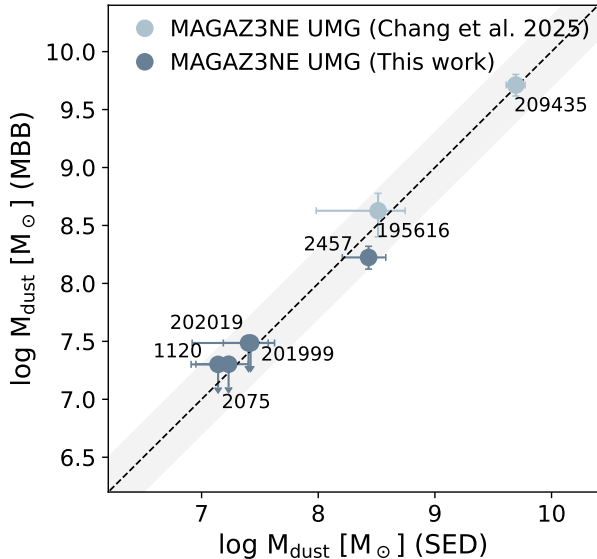


Figure 6. Comparison between dust masses from CIGALE SED fitting and single-temperature modified blackbody fits for five MAGAZ3NE UMGs. The black dashed line is the 1:1 relation, and the grey band marks ± 0.3 dex (a factor of ~ 2) around unity. Source IDs are annotated.

dust mass estimation and stellar mass fitted from the SED fitting using CIGALE. All five UMGs occupy the extreme low end of the $M_{\text{dust}}/M_{\star}$ distribution, with 2 dex below the star-forming scaling relation (L. J. Tacconi et al. 2018). Among them, XMM-VID3-2457 is the only source detected in dust emission, exhibiting the highest $M_{\text{dust}}/M_{\star}$ ratio of $(0.94 \pm 0.17) \times 10^{-3}$. XMM-VID3-1120 and XMM-VID1-2075 fall within the dust-poor orange-shaded region, with $M_{\text{dust}}/M_{\star} < 10^{-4}$, indicating an almost complete depletion of the cold interstellar medium and consistent with their classification as quiescent systems. The remaining two UMGs in the COSMOS field, COS-DR3-202019 and COS-DR3-201999, show the relatively low ratio of $M_{\text{dust}}/M_{\star}$ near 10^{-4} . We include literature measurements of spectroscopically confirmed massive quiescent galaxies at $0.5 < z < 4$, shown as detections with error bars and as upper limits for non-detections. K. E. Whitaker et al. (2021); R. Gobat et al. (2022) confirmed and performed detailed SED fitting for the same lensed quiescent massive galaxies at $1.5 < z < 3.2$, finding $M_{\text{dust}}/M_{\star}$ ratios down to $\sim 10^{-4}$ for a subset of their sample, while others exhibit moderately higher values. J. S. Spilker et al. (2025); J. C. Siegel et al. (2025) identified a small sample of dust-deficient massive quiescent galaxies with only upper limits on dust mass at $0.7 < z < 2.4$. In the higher-redshift range $2.5 < z < 4$, T. L. Suzuki et al. (2022), J. C. Siegel et al. (2025), and H. Umehata et al. (2025) reported quiescent systems with comparatively

higher $M_{\text{dust}}/M_{\star}$ ratios of $2 \times 10^{-4} - 5 \times 10^{-3}$, suggesting that these galaxies are not entirely dust-poor. An exception is ALMA.14 at $z = 1.45$ (M. Hayashi et al. 2018), which exhibits a comparatively high dust-to-stellar mass ratio and may not represent a fully quiescent system (M. M. Lee et al. 2024). Most other massive quiescent galaxies in the literature at $z \gtrsim 3$ remain undetected in dust emission, with detections reported for only 2 of 9 sources and upper limits for the remaining 7 sources.

In Figure 7 (right), we show the dust-to-stellar mass ratio ($M_{\text{dust}}/M_{\star}$) as a function of stellar mass. The UMGs analyzed in this work (black pentagons) lie at the lowest end of the distribution, with $M_{\text{dust}}/M_{\star} < 10^{-4}$ for three sources (XMM-VID3-1120, XMM-VID1-2075, and COS-DR3-201999), placing them among the most dust-poor quiescent galaxies identified spectroscopically at $3 < z < 4$. This apparent dust deficiency at $z > 3$ could plausibly reflect rapid dust depletion or removal processes operating in the most massive quiescent galaxies in the early universe. It could provide new observational constraints on dust consumption and quenching processes in the early universe.

To place our results in theoretical models, we compare our measurements with predictions from the SIMBA cosmological simulation (R. Davé et al. 2019) in Figure 8. We select galaxies from multiple snapshots spanning $3 < z \lesssim 3.5$ of the $(100 h^{-1} \text{Mpc})^3$ simulation box and restrict the sample to massive systems with $\log(M_{\star}/M_{\odot}) > 10$. The selected galaxies are divided into bins of specific star formation rate: $\log(\text{sSFR}/\text{yr}^{-1}) > -9$, $-10 < \log(\text{sSFR}/\text{yr}^{-1}) \leq -9$, and $\log(\text{sSFR}/\text{yr}^{-1}) \leq -10$, with the lowest sSFR bin corresponding to the quiescent population. SIMBA derived $M_{\text{dust}}/M_{\star}$ ratio depends on sSFR, with a broad dispersion in the lowest-sSFR bin. Four non-detected quiescent UMGs in this work lie at the extreme high-mass end ($\log(M_{\star}/M_{\odot}) > 11.3$) of the simulated SIMBA quiescent population. While they show broad agreement with the predicted trends of $M_{\text{dust}}/M_{\star}$ in the quiescent population, four UMGs occupy a region that remains sparsely sampled in current simulations at $3 < z \lesssim 3.5$, effectively extending the parameter space sampled by SIMBA. In contrast, MQGs observed with ALMA continuum in the literature with similar redshifts (R. Gobat et al. 2022; T. L. Suzuki et al. 2022; H. Umehata et al. 2025) exhibit elevated $M_{\text{dust}}/M_{\star}$ ratios relative to the SIMBA median, even though the majority of these MQGs are non-detections. This suggests that they represent quiescent galaxies at an earlier stage of the quenching process, retaining modest dust reservoirs despite their low sSFRs.

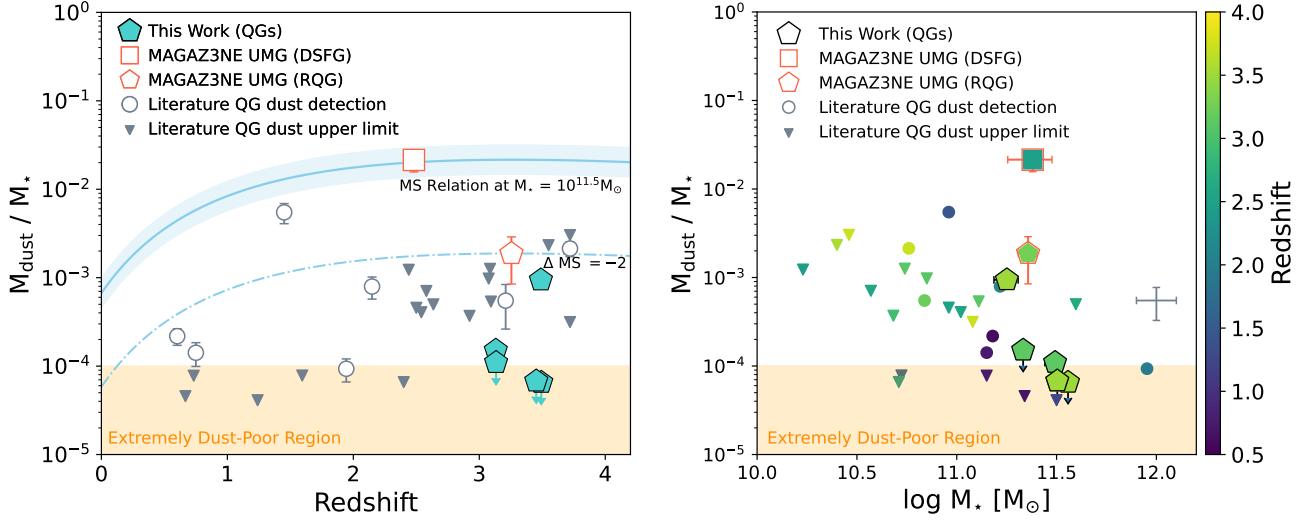


Figure 7. Dust mass fraction ($M_{\text{dust}}/M_{\star}$) of massive quiescent galaxies as a function of redshift (left) and stellar mass (right). Five UMGs analyzed in this work are shown as filled cyan pentagons in the left panel (black outlined pentagons in the right), together with two MAGAZ3NE UMGs with ALMA Band 7 detections (red square for one dusty star-forming galaxy and red pentagon for one recent quenching galaxy; W. Chang et al. 2025). Spectroscopically confirmed massive quiescent galaxies from the literature (R. Gobat et al. 2022; T. L. Suzuki et al. 2022; H. Umehata et al. 2025; J. S. Spilker et al. 2025; J. C. Siegel et al. 2025) are shown as open circles when detected in dust emission and as inverted triangles when only upper limits are available. In the right panel, the literature galaxies are color-coded by redshift, and the gray cross indicates the median uncertainties in stellar mass and the dust-to-stellar mass ratio. The blue shaded region in the left panel represents the main-sequence (MS) scaling relation at $M_{\star} = 10^{11-12} M_{\odot}$ from L. J. Tacconi et al. (2018), and the blue dash-dotted line shows galaxies offset by $\Delta \text{MS} = -2$. The orange-shaded region shows the extremely dust-poor regime with $M_{\text{dust}}/M_{\star} = 10^{-5} - 10^{-4}$.

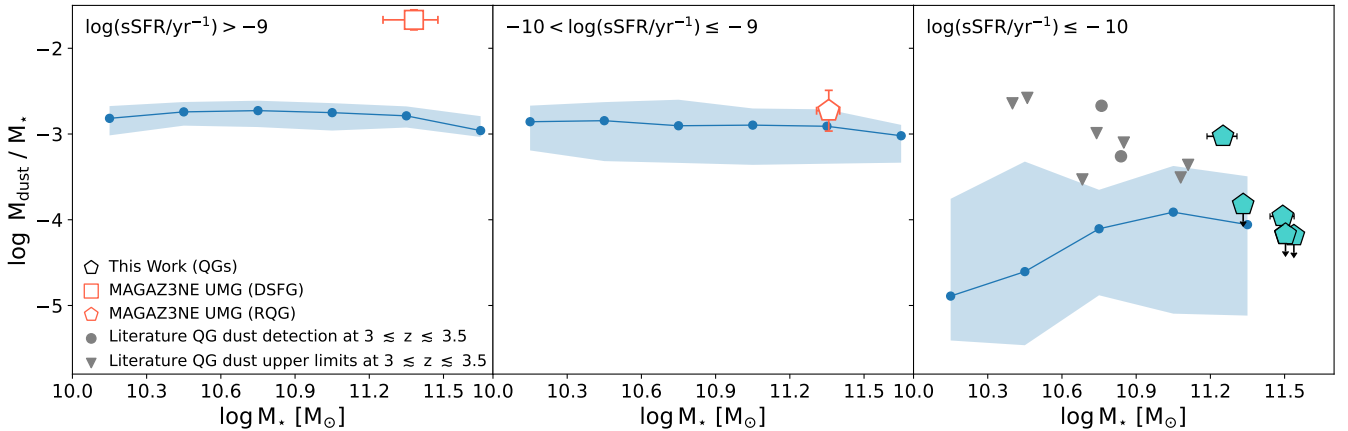


Figure 8. Dust-to-stellar mass ratio as a function of stellar mass for UMGs at $3 \leq z \leq 3.5$, separated into three bins of specific star-formation rate: $\log(\text{sSFR}/\text{yr}^{-1}) > -9$ (left), $-10 < \log(\text{sSFR}/\text{yr}^{-1}) \leq -9$ (middle), and $\log(\text{sSFR}/\text{yr}^{-1}) \leq -10$ (right). Blue points and shaded regions indicate the median and the 16th-84th percentile range of $\log(M_{\text{dust}}/M_{\star})$ in each stellar-mass bin from the SIMBA simulation described in Section 5.3. Grey symbols represent individual massive quiescent galaxies from the literature observed with ALMA at $3 \lesssim z \lesssim 3.5$ (R. Gobat et al. 2022; T. L. Suzuki et al. 2022; H. Umehata et al. 2025), with inverted triangles indicating upper limits, same as Figure 7. MAGAZ3NE UMGs in this work are shown as filled cyan pentagons with two UMGs (red open square for one dusty star-forming galaxy and red open pentagon for one recent quenching galaxy) in W. Chang et al. (2025).

The low dust detection fraction complicates gas-mass estimates based on dust emission. Recent studies have reported unusually high gas-to-dust ratios, reaching values up to 1000 times in massive quiescent galaxies at $0.5 < z < 1.3$ (J. S. Spilker et al. 2025), suggesting that the conversion from dust mass to gas mass carries significant uncertainty. The commonly adopted assumption of a constant gas-to-dust ratio of ~ 100 may therefore be unreliable in the absence of direct constraints, even for high-redshift systems, making gas-mass estimation particularly challenging for dust-deficient galaxies such as the UMGs presented here. Further constraints from direct molecular gas tracers, such as CO or [CI] line observations, are thus essential for accurately determining gas masses and verifying whether these galaxies are truly gas-poor or instead exhibit atypically high gas-to-dust ratios.

6. CONCLUSIONS

In this work, we presented the ALMA observation with Band 7 dust continuum for five UMGs at $z > 3$ in the MAGAZ3NE survey. All five UMGs are located within the quiescent region of the UVJ diagram. Only one galaxy, XMM-VID3-2457, exhibits a faint ALMA Band 7 continuum detection, while the remaining four are undetected down to a sensitivity of $\sigma_{RMS} = 18.6 \mu\text{Jy beam}^{-1}$.

By incorporating ALMA constraints into the CIGALE analysis, we derived reliable stellar, dust, and star-formation properties for five UMGs. Our results confirm that the UV-NIR-selected galaxies are not heavily obscured star-forming systems but lie more than one dex below the star-forming main sequence with $\log(\text{sSFR/Gyr}^{-1}) < -1$, consistent with strongly suppressed star formation as the quiescent galaxies. We further find evidence for AGN activity in a subset of this quiescent sample, including two radio-loud galaxies, while the remaining systems show weak or no AGN signatures.

We estimate dust masses using both SED modeling and modified blackbody fitting, with consistent results between the two methods. The dust-to-stellar mass ratios of our UMGs are more than two dex below the scaling relation for the main-sequence galaxies. The ALMA-detected UMG, XMM-VID3-2457, remains relatively dust-rich with $M_{\text{dust}}/M_{\star} \sim 10^{-3}$. Four UMGs fall in or near the extremely dust-poor, with $M_{\text{dust}}/M_{\star} \lesssim 10^{-4}$, indicating severe dust depletion during the quenching

phase. These values are comparable to or lower than those of spectroscopically confirmed massive quiescent galaxies reported in the literature, placing our sample among the extremely dust-poor systems known at $3 < z < 4$. We compare our results with the SIMBA simulation across different star-formation activity bins at $3 < z \lesssim 3.5$ and find that while our four quiescent UMGs show broad agreement with predicted trends, they occupy a high-mass region with $\log(M_{\star}/M_{\odot}) > 11.3$ that remains sparsely sampled.

This work reveals a significant dust deficiency in the most massive quiescent galaxies at $z > 3$, showing that the dust reservoir may have been depleted more rapidly during the quenching process than previously thought. With the deep ALMA constraints, we show that dust-poor UMGs can be robustly distinguished from heavily obscured star-forming systems, even at the highest stellar masses. Our findings could provide new observational constraints on rapid dust-removal processes during early quenching, where these processes remain poorly explored in simulations of the most massive galaxies.

ACKNOWLEDGMENTS

The authors wish to recognize and acknowledge the very significant cultural role and reverence that the summit of Maunakea has always had within the indigenous Hawaiian community. We are most fortunate to have the opportunity to conduct observations from this mountain. Based on data products from observations made with ESO Telescopes at the La Silla Paranal Observatory under ESO programme ID 179.A-2005 and on data products produced by CALET and the Cambridge Astronomy Survey Unit on behalf of the UltraVISTA consortium.

GW gratefully acknowledges support from the National Science Foundation through grant AST-2347348. BF acknowledges support from JWST-GO-02913.001-A. AM acknowledges support from the Yavin Family Fund. This work is supported by grant number 80NSSC21K0630 issued through the NASA Astrophysics Data Analysis Program (ADAP) and by the National Science Foundation through grant AST-2009442.

Software: astropy (Astropy Collaboration et al. 2013, 2018, 2022), CIGALE M. Boquien et al. (2019); G. Yang et al. (2020, 2022)

APPENDIX

Table A.1. CIGALE modules and input parameters for the SED fitting.

Module	Parameter	Name in CIGALE	Values
Delayed SFH	e-folding time of main population	tau_main	100, 150, 300, 500, 1000, 3000 Myr
	Age of main population	age_main	700, 1000, 1300, 1600 Myr
	Age of the late burst	age_burst	50, 100, 150, 200, 250, 300 Myr
	Mass fraction of the late burst population	f_burst	0.001, 0.005, 0.01, 0.05, 0.1, 0.3
SSP	Initial mass function	imf	Chabrier (2003)
	Stellar metallicity	metallicity	0.02
Nebular emission	Ionization parameter	logU	-4.0, -3.0, -2.0,
	Gas metallicity	z_gas	0.008, 0.014, 0.02, 0.03
Dust attenuation	Color excess of nebular emission lines	E_BV_lines	0, 0.04, 0.07, 0.1, 0.2, 0.3, 0.4, 0.5
	Amplitude of the UV bump	uv_bump_amplitude	0.0, 1, 2, 3
	Slope of the attenuation curve	powerlaw_slope	-2, -1.5, -1, -0.5, 0.0
Dust emission	Mass fraction of PAH	qpah	1.77, 2.5, 3.19
	Minimum radiation field	umin	0.1, 0.5, 1, 1.5, 2, 4, 6, 10
	Powerlaw slope	alpha	1.5, 2, 2.5
	Fraction illuminated from Umin to Umax	gamma	0.01, 0.05, 0.1, 0.2
AGN emission	Inclination	i	30°, 70°
	AGN fraction	fracAGN	0.1–0.9 (step 0.1)
	Extinction in the polar direction	EBV	0.03, 0.1, 0.2, 0.3
Radio ^a	The slope of synchrotron emission	alpha_sf	0.8
	The radio-loudness parameter	R_AGN	0.1, 1, 10, 50, 100, 150, 200

^aThis module is only fitted for UMGs in the COSMOS field (COS-DR3-201999 and COS-DR3-202019).

REFERENCES

Astropy Collaboration, Robitaille, T. P., Tollerud, E. J., et al. 2013, A&A, 558, A33, doi: [10.1051/0004-6361/201322068](https://doi.org/10.1051/0004-6361/201322068)

Astropy Collaboration, Price-Whelan, A. M., Sipőcz, B. M., et al. 2018, AJ, 156, 123, doi: [10.3847/1538-3881/aabc4f](https://doi.org/10.3847/1538-3881/aabc4f)

Astropy Collaboration, Price-Whelan, A. M., Lim, P. L., et al. 2022, ApJ, 935, 167, doi: [10.3847/1538-4357/ac7c74](https://doi.org/10.3847/1538-4357/ac7c74)

Belli, S., Newman, A. B., Ellis, R. S., & Konidaris, N. P. 2014, ApJL, 788, L29, doi: [10.1088/2041-8205/788/2/L29](https://doi.org/10.1088/2041-8205/788/2/L29)

Bezanson, R., Spilker, J., Williams, C. C., et al. 2019, ApJL, 873, L19, doi: [10.3847/2041-8213/ab0c9c](https://doi.org/10.3847/2041-8213/ab0c9c)

Boquien, M., Burgarella, D., Roehlly, Y., et al. 2019, A&A, 622, A103, doi: [10.1051/0004-6361/201834156](https://doi.org/10.1051/0004-6361/201834156)

Bruzual, G., & Charlot, S. 2003, MNRAS, 344, 1000, doi: [10.1046/j.1365-8711.2003.06897.x](https://doi.org/10.1046/j.1365-8711.2003.06897.x)

Bugiani, L., Belli, S., Park, M., et al. 2025, ApJ, 981, 25, doi: [10.3847/1538-4357/adaeaf](https://doi.org/10.3847/1538-4357/adaeaf)

Butler, A., Huynh, M., Delvecchio, I., et al. 2018, A&A, 620, A16, doi: [10.1051/0004-6361/201732379](https://doi.org/10.1051/0004-6361/201732379)

Calzetti, D., Armus, L., Bohlin, R. C., et al. 2000, ApJ, 533, 682, doi: [10.1086/308692](https://doi.org/10.1086/308692)

Carnall, A. C., McLeod, D. J., McLure, R. J., et al. 2023, MNRAS, 520, 3974, doi: [10.1093/mnras/stad369](https://doi.org/10.1093/mnras/stad369)

Chabrier, G. 2003, PASP, 115, 763, doi: [10.1086/376392](https://doi.org/10.1086/376392)

Chang, W., Wilson, G., Forrest, B., et al. 2025, arXiv e-prints, arXiv:2508.08460, doi: [10.48550/arXiv.2508.08460](https://doi.org/10.48550/arXiv.2508.08460)

Davé, R., Anglés-Alcázar, D., Narayanan, D., et al. 2019, MNRAS, 486, 2827, doi: [10.1093/mnras/stz937](https://doi.org/10.1093/mnras/stz937)

de Graaff, A., Setton, D. J., Brammer, G., et al. 2025, Nature Astronomy, 9, 280, doi: [10.1038/s41550-024-02424-3](https://doi.org/10.1038/s41550-024-02424-3)

Draine, B. T., Aniano, G., Krause, O., et al. 2014, ApJ, 780, 172, doi: [10.1088/0004-637X/780/2/172](https://doi.org/10.1088/0004-637X/780/2/172)

Forrest, B., Annunziatella, M., Wilson, G., et al. 2020a, ApJL, 890, L1, doi: [10.3847/2041-8213/ab5b9f](https://doi.org/10.3847/2041-8213/ab5b9f)

Forrest, B., Marsan, Z. C., Annunziatella, M., et al. 2020b, ApJ, 903, 47, doi: [10.3847/1538-4357/abb819](https://doi.org/10.3847/1538-4357/abb819)

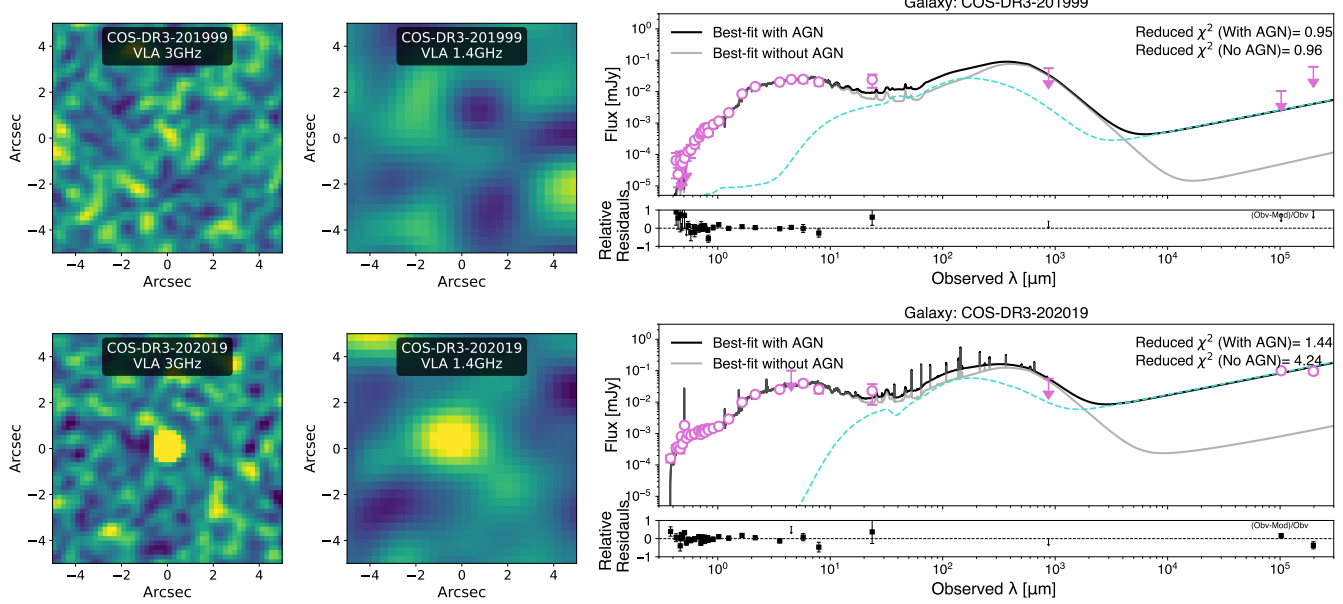


Figure A.1. VLA radio images and UV-to-radio SED modeling for COS-DR3-201999 ($z_{\text{spec}} = 3.131$) and COS-DR3-202019 ($z_{\text{spec}} = 3.133$), shown in the same format as Figure 3. Black and gray curves represent the best-fit models with (black solid line) and without (gray solid line) an AGN component, respectively, with the AGN contribution shown by the cyan dashed curve. The reduced χ^2 values for the fits with and without AGN are listed in the panel titles.

Forrest, B., Wilson, G., Muzzin, A., et al. 2022, ApJ, 938, 109, doi: [10.3847/1538-4357/ac8747](https://doi.org/10.3847/1538-4357/ac8747)

Forrest, B., Cooper, M. C., Muzzin, A., et al. 2024, ApJ, 977, 51, doi: [10.3847/1538-4357/ad8b1c](https://doi.org/10.3847/1538-4357/ad8b1c)

Glazebrook, K., Schreiber, C., Labb  , I., et al. 2017, Nature, 544, 71, doi: [10.1038/nature21680](https://doi.org/10.1038/nature21680)

Gobat, R., D'Eugenio, C., Liu, D., et al. 2022, A&A, 668, L4, doi: [10.1051/0004-6361/202244995](https://doi.org/10.1051/0004-6361/202244995)

Gobat, R., Daddi, E., Magdis, G., et al. 2018, Nature Astronomy, 2, 239, doi: [10.1038/s41550-017-0352-5](https://doi.org/10.1038/s41550-017-0352-5)

Hayashi, M., Tadaki, K.-i., Kodama, T., et al. 2018, ApJ, 856, 118, doi: [10.3847/1538-4357/aab3e7](https://doi.org/10.3847/1538-4357/aab3e7)

Hwang, Y.-H., Wang, W.-H., Chang, Y.-Y., et al. 2021, ApJ, 913, 6, doi: [10.3847/1538-4357/abf11a](https://doi.org/10.3847/1538-4357/abf11a)

Jarvis, M. J., Bonfield, D. G., Bruce, V. A., et al. 2013, MNRAS, 428, 1281, doi: [10.1093/mnras/sts118](https://doi.org/10.1093/mnras/sts118)

Jin, S., Daddi, E., Liu, D., et al. 2018, ApJ, 864, 56, doi: [10.3847/1538-4357/aad4af](https://doi.org/10.3847/1538-4357/aad4af)

Jin, S., Sillassen, N. B., Magdis, G. E., et al. 2024, A&A, 683, L4, doi: [10.1051/0004-6361/202348540](https://doi.org/10.1051/0004-6361/202348540)

Kennicutt, Jr., R. C. 1998, ARA&A, 36, 189, doi: [10.1146/annurev.astro.36.1.189](https://doi.org/10.1146/annurev.astro.36.1.189)

Kubo, M., Umehata, H., Matsuda, Y., et al. 2022, ApJ, 935, 89, doi: [10.3847/1538-4357/ac7f2d](https://doi.org/10.3847/1538-4357/ac7f2d)

Lacy, M., Surace, J. A., Farrah, D., et al. 2021, MNRAS, 501, 892, doi: [10.1093/mnras/staa3714](https://doi.org/10.1093/mnras/staa3714)

Le Floc'h, E., Aussel, H., Ilbert, O., et al. 2009, ApJ, 703, 222, doi: [10.1088/0004-637X/703/1/222](https://doi.org/10.1088/0004-637X/703/1/222)

Lee, M. M., Steidel, C. C., Brammer, G., et al. 2024, MNRAS, 527, 9529, doi: [10.1093/mnras/stad3718](https://doi.org/10.1093/mnras/stad3718)

Li, A., & Draine, B. T. 2001, ApJ, 554, 778, doi: [10.1086/323147](https://doi.org/10.1086/323147)

Marsan, Z. C., Marchesini, D., Brammer, G. B., et al. 2017, ApJ, 842, 21, doi: [10.3847/1538-4357/aa7206](https://doi.org/10.3847/1538-4357/aa7206)

Marsan, Z. C., Muzzin, A., Marchesini, D., et al. 2022, ApJ, 924, 25, doi: [10.3847/1538-4357/ac312a](https://doi.org/10.3847/1538-4357/ac312a)

Mauduit, J. C., Lacy, M., Farrah, D., et al. 2012, PASP, 124, 1135, doi: [10.1086/668290](https://doi.org/10.1086/668290)

McConachie, I., Wilson, G., Forrest, B., et al. 2022, ApJ, 926, 37, doi: [10.3847/1538-4357/ac2b9f](https://doi.org/10.3847/1538-4357/ac2b9f)

McConachie, I., Wilson, G., Forrest, B., et al. 2025, ApJ, 978, 17, doi: [10.3847/1538-4357/ad8f36](https://doi.org/10.3847/1538-4357/ad8f36)

McCracken, H. J., Milvang-Jensen, B., Dunlop, J., et al. 2012, A&A, 544, A156, doi: [10.1051/0004-6361/201219507](https://doi.org/10.1051/0004-6361/201219507)

Muzzin, A., Marchesini, D., Stefanon, M., et al. 2013, ApJS, 206, 8, doi: [10.1088/0067-0049/206/1/8](https://doi.org/10.1088/0067-0049/206/1/8)

Nanayakkara, T., Glazebrook, K., Schreiber, C., et al. 2025, ApJ, 981, 78, doi: [10.3847/1538-4357/ada6ac](https://doi.org/10.3847/1538-4357/ada6ac)

Oke, J. B., & Gunn, J. E. 1983, ApJ, 266, 713, doi: [10.1086/160817](https://doi.org/10.1086/160817)

Saracco, P., Marchesini, D., La Barbera, F., et al. 2020, ApJ, 905, 40, doi: [10.3847/1538-4357/abc7c4](https://doi.org/10.3847/1538-4357/abc7c4)

Schinnerer, E., Sargent, M. T., Bondi, M., et al. 2010, ApJS, 188, 384, doi: [10.1088/0067-0049/188/2/384](https://doi.org/10.1088/0067-0049/188/2/384)

Schreiber, C. 2023, cschreib/slinefit, v2.3 GitHub. <https://github.com/cschreib/slinefit>

Schreiber, C., & Dickinson, H. 2023, cschreib/fastpp, v1.5.0 GitHub. <https://github.com/cschreib/fastpp>

Schreiber, C., Labb  , I., Glazebrook, K., et al. 2018a, *A&A*, 611, A22, doi: [10.1051/0004-6361/201731917](https://doi.org/10.1051/0004-6361/201731917)

Schreiber, C., Glazebrook, K., Nanayakkara, T., et al. 2018b, *A&A*, 618, A85, doi: [10.1051/0004-6361/201833070](https://doi.org/10.1051/0004-6361/201833070)

Scoville, N., Aussel, H., Brusa, M., et al. 2007, *ApJS*, 172, 1, doi: [10.1086/516585](https://doi.org/10.1086/516585)

Scoville, N., Aussel, H., Sheth, K., et al. 2014, *ApJ*, 783, 84, doi: [10.1088/0004-637X/783/2/84](https://doi.org/10.1088/0004-637X/783/2/84)

Siegel, J. C., Setton, D. J., Greene, J. E., et al. 2025, *ApJ*, 985, 125, doi: [10.3847/1538-4357/adc7b7](https://doi.org/10.3847/1538-4357/adc7b7)

Smolci  , V., Novak, M., Bondi, M., et al. 2017, *A&A*, 602, A1, doi: [10.1051/0004-6361/201628704](https://doi.org/10.1051/0004-6361/201628704)

Spilker, J. S., Whitaker, K. E., Narayanan, D., et al. 2025, arXiv e-prints, arXiv:2507.16914, doi: [10.48550/arXiv.2507.16914](https://doi.org/10.48550/arXiv.2507.16914)

Stalevski, M., Fritz, J., Baes, M., Nakos, T., & Popovi  , L.   . 2012, *MNRAS*, 420, 2756, doi: [10.1111/j.1365-2966.2011.19775.x](https://doi.org/10.1111/j.1365-2966.2011.19775.x)

Stalevski, M., Ricci, C., Ueda, Y., et al. 2016, *MNRAS*, 458, 2288, doi: [10.1093/mnras/stw444](https://doi.org/10.1093/mnras/stw444)

Suzuki, T. L., Glazebrook, K., Schreiber, C., et al. 2022, *ApJ*, 936, 61, doi: [10.3847/1538-4357/ac7ce3](https://doi.org/10.3847/1538-4357/ac7ce3)

Tacconi, L. J., Genzel, R., Saintonge, A., et al. 2018, *ApJ*, 853, 179, doi: [10.3847/1538-4357/aaa4b4](https://doi.org/10.3847/1538-4357/aaa4b4)

Tomczak, A. R., Quadri, R. F., Tran, K.-V. H., et al. 2016, *ApJ*, 817, 118, doi: [10.3847/0004-637X/817/2/118](https://doi.org/10.3847/0004-637X/817/2/118)

Umeshita, H., Kubo, M., & Nakanishi, K. 2025, *ApJL*, 985, L8, doi: [10.3847/2041-8213/add1d4](https://doi.org/10.3847/2041-8213/add1d4)

Urbano Stawinski, S. M., Cooper, M. C., Forrest, B., et al. 2024, *The Open Journal of Astrophysics*, 7, 46, doi: [10.33232/001c.120087](https://doi.org/10.33232/001c.120087)

Weaver, J. R., Kauffmann, O. B., Ilbert, O., et al. 2022, *ApJS*, 258, 11, doi: [10.3847/1538-4365/ac3078](https://doi.org/10.3847/1538-4365/ac3078)

Whitaker, K. E., Labb  , I., van Dokkum, P. G., et al. 2011, *ApJ*, 735, 86, doi: [10.1088/0004-637X/735/2/86](https://doi.org/10.1088/0004-637X/735/2/86)

Whitaker, K. E., Williams, C. C., Mowla, L., et al. 2021, *Nature*, 597, 485, doi: [10.1038/s41586-021-03806-7](https://doi.org/10.1038/s41586-021-03806-7)

Yang, G., Boquien, M., Buat, V., et al. 2020, *MNRAS*, 491, 740, doi: [10.1093/mnras/stz3001](https://doi.org/10.1093/mnras/stz3001)

Yang, G., Boquien, M., Brandt, W. N., et al. 2022, *ApJ*, 927, 192, doi: [10.3847/1538-4357/ac4971](https://doi.org/10.3847/1538-4357/ac4971)